Detuning Axis Pulsed Spectroscopy of Valley-Orbital States in Si/Si-Ge Quantum Dots

Edward H. Chen[●],[†] Kate Raach[●],[*] Andrew Pan, Andrey A. Kiselev, Edwin Acuna, Jacob Z. Blumoff,
Teresa Brecht, Maxwell D. Choi, Wonill Ha, Daniel R. Hulbert[●], Michael P. Jura, Tyler E. Keating,
Ramsey Noah[●], Bo Sun, Bryan J. Thomas, Matthew G. Borselli[●], C.A.C. Jackson,
Matthew T. Rakher, and Richard S. Ross

HRL Laboratories LLC, 3011 Malibu Canyon Road, Malibu, California 90265, USA

Silicon-quantum-dot qubits must contend with low-lying valley excited states that are sensitive functions of the quantum-well heterostructure and disorder; quantifying and maximizing the energies of these states are critical to improving device performance. We describe a spectroscopic method for probing excited states in isolated Si/Si-Ge double quantum dots using standard baseband pulsing techniques, easing the extraction of energy spectra in multiple-dot devices. We use this method to measure dozens of valley excited-state energies spanning multiple wafers, quantum dots, and orbital states, which are crucial for evaluating the dependence of valley splitting on quantum well width and other epitaxial conditions. Our results suggest that narrower wells can be beneficial for increasing valley splittings, but this effect can be confounded by variations in growth and fabrication conditions. These results underscore the importance of valley-splitting measurements for guiding the development of Si qubits.

I. INTRODUCTION

Electrostatically confined quantum-dot (QD) spin qubits in Si/Si-Ge quantum wells (QWs) are a promising platform for processing quantum information [1,2]. The valleys inherent to the Si band structure, however, can fundamentally limit the initialization, manipulation, and measurement fidelities of qubit states [3]. In a typical Si/Si-Ge QW design, tensile strain and spatial quantization partially break the sixfold degeneracy of the bulk Si conduction band, leaving the two-lowest out-of-plane valleys. This remaining degeneracy can be lifted by sharp disruptions of the periodic crystal potential at the QW interfaces. Measuring, understanding, and increasing the resulting valley-splitting (VS) energy is critical for improving qubit performance.

Despite the importance of VS, there is not a consensus on the best method of measuring VS in silicon QDs. Shubnikov–de Haas measurements are commonly used to extract the energy spectrum, including valley states, of two-dimensional electron gases induced in QWs [4–7]. However, these macroscopic ensemble measurements average over epitaxial disorder, magnetic confinement, and many-body effects, and hence their quantitative relevance to individual single-electron QDs is not clear.

A number of techniques for directly probing QD energy levels have been demonstrated with assorted advantages and limitations. Measurements of QD conductance can yield information about level spacings [8], but are complicated for multi-QD devices not designed for transport. rf-based techniques, such as photon-assisted tunneling or resonant-cavity response of double quantum dots (DQDs), can drive intervalley transitions precisely, but are typically limited by the maximum frequency of microwave photons that can be reliably delivered to the device [9,10]. Pulsed-gate spectroscopy, by contrast, does not require microwave control and has been used to probe valley and other excited QD states in a variety of systems [11]. This can be used in concert with large external magnetic fields to perform magnetospectroscopy (measuring valley-limited two-electron singlet-triplet splittings, for instance) [12] or to extract single-electron VS via spin-valley hotspot effects [13]. However, conventional QD pulsed-gate techniques [14,15] rely on the detuning dependence of the tunneling rate with a neighboring electron bath, similarly to transport-based measurements. This restricts the range of allowable QD biasing and can complicate the spectral interpretation when weakly quantized bath excitations induce additional resonant features [8,16]. Overall, commonly used techniques require devices to be designed or tuned in ways that differ significantly from ideal coherent operation, making it harder to characterize the dot-to-dot and device-to-device behavior of VS in extensible designs.

---

*cmraach@hrl.com
†Present address: IBM Almaden Research Center, 650 Harry Road, San Jose, California 95120, USA.

Nonetheless, using the methods mentioned above as well as other methods [17–19], various groups have reported a wide range of valley splittings between 10 and 270 μeV in Si/Si-Ge QDs. The large variation is commonly assumed to be related to the QW epitaxy, although further insight is difficult as values are typically reported for just one or two QDs.

Valley splitting is sensitive to the overlap of the confined electron wave function with the Si/Si-Ge epitaxial heterointerfaces, and is therefore expected to increase with better interfaces, narrower quantum wells, and/or stronger electric fields [20–24]. Similarly, interfacial disorder originating from steps, atomic interdiffusion, intrinsic alloy randomness, and other sources is expected to affect valley-splitting energies realized by electrons in different orbital states [25,26]. Disorder also introduces valley-orbit mixing [27], which is responsible for coupling valley states belonging to different orbitals. Thus, strictly speaking, the resulting electron eigenstates are commonly mixed, (i.e., valley-orbit in character). Both measurements and modeling of our devices suggest the orbital energies are on the 1-meV scale, whereas the valley energies are on the 10–100-μeV scale. When the energetics of orbital confinement strongly dominate valley mixing, it is appropriate to distinguish mostly orbital and mostly valley states and excitations, with an unambiguous structure of low-energy levels [3] emerging as a result. Reliable valley-splitting measurements across a range of QDs and devices are necessary for disentangling these effects.

In this paper, we introduce an experimental technique for measuring the excited-state energy spectra of pairs of QDs. This method, which we call "detuning axis pulsed spectroscopy" (DAPS), can be applied to any charge configuration, but we focus primarily on the single-electron case, for which the spectra are most easily understood. This allows us to systematically probe multiple valley and orbital states of individual dots in Si/Si-Ge QWs with various widths and growth conditions. Our results validate the scalability of the DAPS technique and emphasize the importance of epitaxial uniformity for controlling the valley splitting in QD devices.

II. EXPERIMENTAL SETUP

Our experiments use single electrons trapped within arrays of accumulation-mode, Si/Si-Ge QDs designed to form a pair of exchange-only qubits [28–30]. An example of such a device in an overlapping Al-gate layout [31] is shown in Fig. 1(a). The quantum dots form within an isotopically purified (800-ppm) Si QW embedded in a strain-relaxed, undoped Si-Ge alloy. Large field gates (not visible) surrounding the quantum-dot region prevent the accumulation of electrons around the device perimeter. Six plunger gates labeled as P1 through P6 control the chemical potential within each dot, while five exchange gates
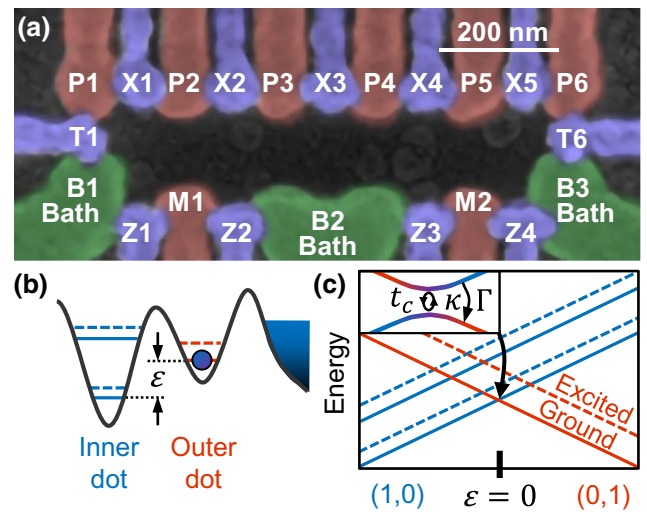

FIG. 1. (a) Scanning electron micrograph of a six-QD accumulation-mode device layout typical of those used in this study. Readout is done via the M1 and M2 QDs biased to the Coulomb-blockade regime to measure the charge configuration. (b) Low-energy excited states of a DQD; each orbital excitation (solid lines) has an associated valley excitation (dashed lines). The detuning energy ε is the primary degree of freedom for extracting energy splittings in the DAPS technique. (c) The DQD energy-level diagram along the detuning axis. The inset shows the vicinity of a level anticrossing, where the charge-transfer dynamics are strongly impacted by the tunnel coupling t_c and interdot dephasing and relaxation rates, κ and Γ.

labeled as X1 through X5 modulate the interdot tunneling rates and exchange interactions. Two additional tunneling gates labeled as T1 and T6 control the tunneling rates of electrons into dots P1 and P6 from reservoirs B1 and B3, respectively. Two dot charge sensors formed underneath gates M1 and M2 are used for measuring charge configurations of the six-dot array. For coherent operations, the six electrons comprise two triple-quantum-dot exchange-only qubits, which can be fully controlled by only baseband voltage pulses and do not require external magnetic fields or rf control. It is therefore advantageous to characterize the level spectrum in the same way, which is one technical advantage of our approach.

In devices such the one pictured here, most QDs are far from a neighboring electron bath. When we characterize a DQD pair, therefore, we generically refer to the QD closer to the nearest electron bath as the "outer dot" and the more distant QD as the "inner dot," as sketched in Fig. 1(b). Here we also schematically depict the simplest case for QD low-energy states with each orbital (solid lines) having an associated valley excitation (dashed lines). The DQD energy spectrum as a function of dot detuning resembles the spectrum in Fig. 1(c), and our measurement method relies on mapping the anticrossings between excited levels of the different dots.

III. DAPS TECHNIQUE

The DAPS technique probes the DQD energy spectra by preparing electrons in the ground state of one dot and tracking charge transitions to the other dot as a function of detuning across the (1,0)-(0,1) charge boundary. Energies are extracted by our identifying level anticrossings at particular detunings, as indicated in Fig. 1(c), on the basis of enhanced charge-transition rates at those biases. This requires only standard baseband control, without the need for rf or magnetic fields, and improves on standard pulsed-gate spectroscopy [11] by probing multiple dots without requiring direct coupling to an electron bath. We illustrate the experimental procedure in Figs. 2(a) and 2(b) using the (1,0)-(0,1) transition of a DQD, formed in this case underneath gates P2 and P3 in a device like that in Fig. 1(a). Figure 2(a) shows the charge-stability diagram for the DQD, where the M1-dot-charge-sensor conductance is measured while the voltage biases applied to the P2 and P3 gates are swept. The dots are in the low-tunnel-coupling regime we use to perform DAPS, where the loading rates are slower than our scan rate. The expected charge-cell boundaries become clearer at higher tunnel coupling as illustrated in the inset. The charge-stability diagram is labeled with the three bias points A, B, and C we perform cycling between for the experiment. At point A near the (1,0) loading line, we prepare the electron in the ground state of the outer dot (here, P2); this can be done by waiting for thermalization within the charge cell, although we accelerate this process by allowing electron exchange with a neighboring bath extended by our biasing the P1 QD to the same chemical potential as bath B1 [32]. The electron is then pulsed to point B, where the nearest dot charge sensor, either M1 or M2, is measured to record a reference conductance for the (1,0) charge state. A diabatic [33] pulse takes the electron, its state unchanged, to point C along the detuning axis, ε, across the charge boundary, where it is held for time t_{hold} before returning rapidly to point B for another charge-state measurement. This second measurement is compared with the reference to obtain a differential signal.

Sweeping the detuning position C and t_{hold} allows us to map out the charge decay dynamics, as shown in Fig. 2(c). Two orbital excited states (empty circle: ground valley; filled circle: excited valley) are resolved as peaks for $t_{\text{hold}} = 100$ ns, but become indistinguishable for $t_{\text{hold}} = 10~\mu$s due to rapid interdot relaxation at large detuning. In contrast, the two orbital ground states (empty triangle: ground valley; filled triangle: excited valley) remain well resolved for both hold times. These four transitions resemble states of the inner dot illustrated in Fig. 1(b). The detuning voltage is translated to energy with use of the measured gate-lever-arm matrix [16,17]. Experimental uncertainties in the lever-arm measurements constitute a primary source of systematic error; for devices that show a
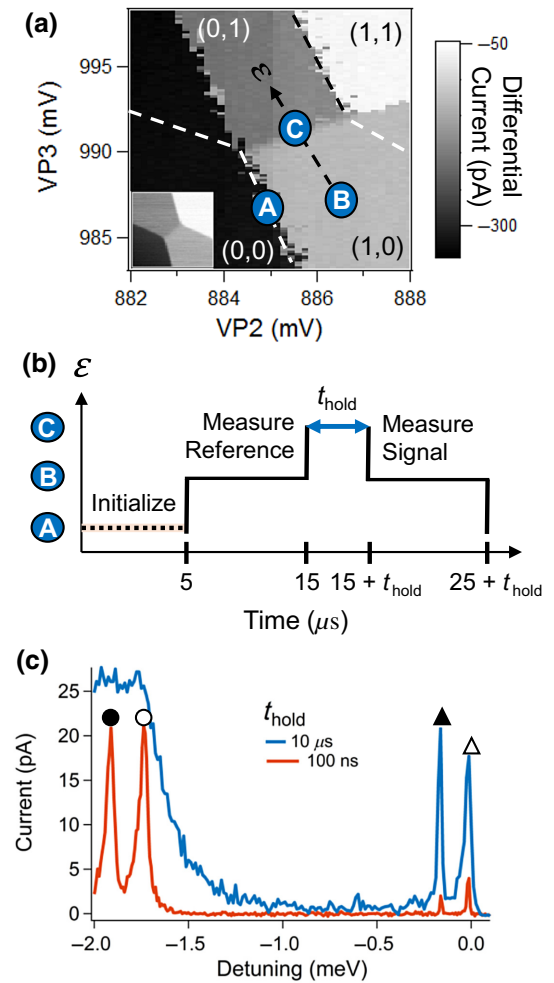

FIG. 2. (a) Measured charge-stability diagram of a P2-P3 DQD in the low-tunnel-coupling regime. Relevant bias locations for the DAPS measurement are overlaid; the line along B-C defines the detuning axis parameterized by ε. The inset shows a typical charge-stability diagram obtained at higher tunnel coupling, which has the expected honeycomb charge-cell shape. (b) Pulse timing sequence for DAPS. A 5-μs initialization at A is followed by a 10-μs charge reference measurement at B. Then the bias moves to the swept position C for a duration t_{hold} before a final charge measurement at B lasting 10 μs. (c) P3 DAPS measurement of differential current versus detuning energy (inferred from voltages with use of the measured capacitance matrix) for two hold times: 100 ns (orange) and 10 μs (blue). Empty circle, ground valley; filled circle, excited valley; empty triangle, ground valley; filled triangle, excited valley.

microwave response, auxiliary rf measurements can reduce this uncertainty by providing a definite voltage-to-energy scale, as illustrated in Appendix A. The procedure may be extended to probe the other, outer dot (P2 in this example) by preparing the electron at A and adiabatically ramping across the charge boundary to the (0,1) charge cell, from where diabatic detuning excursions toward (1,0) can be used to determine the spectrum of the P2 dot.

The DAPS sequence resembles standard charge-qubit-control techniques, and its main features can be described by a Lindblad master equation (analyzed in detail in Appendix B), where the most-relevant quantities are the interdot tunnel coupling t_c, charge dephasing κ, and the interdot inelastic relaxation rate Γ, as sketched in Fig. 1(c). However, coherent charge manipulation requires large tunnel coupling (much greater than 1 GHz) and hence ultrafast control. While nonadiabatic pulses can be used to coherently probe excited states by means of Landau-Zener interferometry [18,34], its extreme sensitivity to tunnel coupling and the pulse waveform makes it an unwieldy method to optimize for spectroscopy. Instead, we find the low-tunnel-coupling regime to be most desirable for DAPS because it maintains the diabaticity of detuning pulses, ensuring all charge transitions occur during the hold step [point C in Fig. 2(b)]. In this incoherent regime, when the DQD is detuned at an interdot level crossing, charge transitions occur at a rate approximately equal to t_c^2/κ, where both t_c and κ can range from 10^7 to 10^{10} s^{-1}. These longer timescales are easily probed with typical control hardware for exchange-only operation, which requires bandwidths in the 0.1-1.0-GHz range [29]. To resolve these transitions, hold times should be kept short to prevent inelastic decay ($\Gamma \approx 10^3$–10^8 s^{-1}) from equilibration of the DQD. The measurement steps at point B must also be done faster than Γ to resolve the signal. This implies that DAPS should be performed for $\kappa t_c^{-2} < t_{\text{hold}} < \Gamma^{-1}$. Meeting these criteria requires tuning of both the tunnel barrier and t_{hold}, since t_c varies for excited states and the inelastic decay rate may itself be a function of detuning and tunnel coupling. As

one example, the excited orbital states at large detuning on the left-hand side of Fig. 2(c) are clear only at small t_{hold} and are unresolved at longer times due to their faster thermalization rates.

IV. VALLEY-ORBITAL SPECTROSCOPY RESULTS

Using the DAPS method, we can quantify the valley-orbit level structure of Si/Si-Ge QDs in more detail than is usually reported. As an example, Figs. 3(a) and 3(b) depict the measured charge-transition probabilities of a P5-P6 DQD versus detuning energy and hold time. We obtain the probability by averaging over single-shot DAPS measurements at each detuning and t_{hold}, where a charge transition is registered if the differential current between the signal and reference measurements surpasses a specified threshold. Since the (1,0) and (0,1) charge states have substantially different conductance signals, the binning of charge states can be performed accurately by standard QD-readout procedures [17]. Resonant peaks are identified in Figs. 3(c) and 3(d) from fitted exponential decay rates as a function of detuning, which we then associate with the level crossings illustrated in Figs. 3(e) and 3(f). Table I lists the extracted energies and tentative assignments to mostly valley or mostly orbital states based on the splitting magnitudes and transition strengths. In particular, the lowest excited-valley transitions exhibit decay times roughly 10 times longer than the ground-valley transitions in Figs. 3(c) and 3(d), suggestive of a
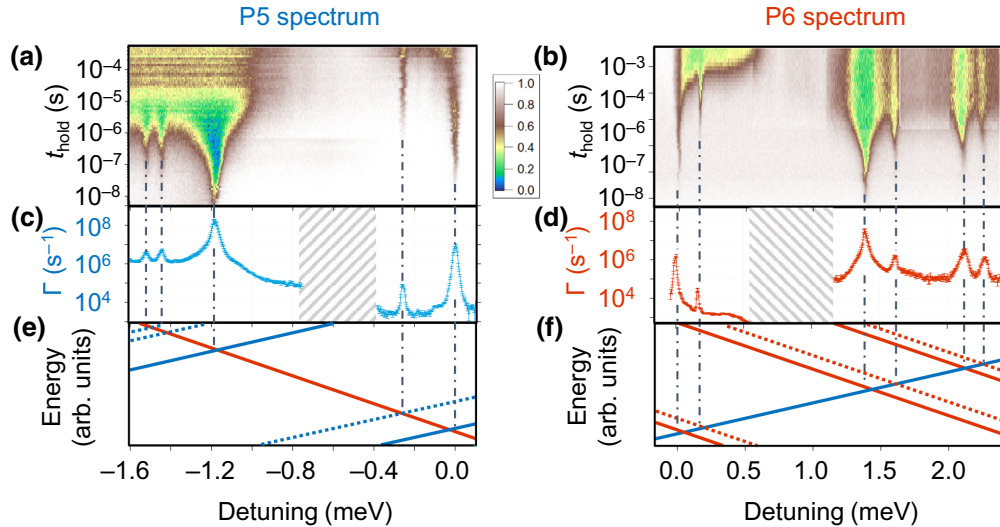

FIG. 3. DAPS charge-decay measurements of a P5-P6 DQD as a function of detuning ε and hold time t_{hold} for (a) the inner dot P5 and (b) the outer dot P6. The color scale indicates the probability of the electron remaining in its initial charge state. (c),(d) Charge decay rates Γ versus detuning extracted from exponential fits of each column of the data in (a),(b). (e),(f) Simplified energy-level diagrams with regard to detuning for the P5 (blue lines) and P6 (red lines) QDs. Notably, for each orbital in a dot, the valley ground state (solid line) tends to decay faster than its valley excited counterpart (dotted line). A possible exception is the set of higher excited P5 orbital or valley states in the upper left of (e), as further discussed in the main text.

TABLE I. Extracted peak energies and assigned valley splittings for different orbital excitations for dots P5 and P6 based on Lorentzian fits to the data in Fig. 3. All energies are in the unit of microelectronvolts. An asterisk for selected P5 data denotes the uncertain interpretation of those peaks, as discussed in the main text.

Orbital assignment	P5			P6		
	Ground valley peak	Excited valley peak	Valley splitting	Ground valley peak	Excited valley peak	Valley splitting
Ground	2 ± 7	-258 ± 9	260 ± 11	-1 ± 8	161 ± 6	162 ± 10
First excited	-1184 ± 14	-1445 ± 12	261 ± 14	1393 ± 12	1615 ± 22	222 ± 23
Second excited	NA*	-1520 ± 13	$336 \pm 15^*$	2125 ± 23	2275 ± 26	150 ± 27

3 times or greater reduction of the intervalley tunnel coupling due to differences in the interdot valley phase [35]. This pattern also recurs for several higher excited states in P5 and P6 dots, providing further motivation for our valley-orbit assignments. This observation is consistent, for example, with a primarily flat heterointerface without steps, although by itself it is not sufficient to characterize the interface quality. Nonetheless, these labels can be ambiguous at high energies where multiple valley-orbit excitations are present. This is particularly so for P5, where only one "orbital-like" excited state with a fast decay is observed, accompanied by twin "valley-like" states with slower decay rates. To reiterate, only a single valley-like excitation per orbital is expected in our Si-Ge devices with large built-in biaxial tensile strain in the Si layer. The dual slow peaks could be because another state overlaps or otherwise hybridizes with the visible levels, or possibly because it lies beyond the probed energy range. Indeed, one of those twin peaks could actually be a manifestation of the second excited orbital, with its decay rate observed, as expected, to be highly suppressed, likely by symmetry, relative to the first excited orbital; this latter pattern is consistent with the structure of the higher excited peaks observed in the P6 spectrum in Figs. 3(b), 3(d), and 3(f). Alternatively, a slower second-excited-orbital peak in P5 could be masked by a much-faster decay into the close-in-energy first excited orbital. This possibility seems less plausible in view of the comparable decay rates of the accompanying twin peaks and orbital semidegeneracy that would indicate an accidental approximate axial symmetry of the in-plane confinement. The substantially differing orbital splittings of P6 imply asymmetry in the confining potential (see Sec E.2 in Ref. [3] and Ref. [17] for an in-depth discussion of the confinement symmetry effects on the dot energy spectrum).

The precise detuning location of the transition peaks can vary depending on the charge dynamics, as discussed in Appendix C; however, these shifts are typically small in scale, and so energy splittings (peak separations) can be reliably extracted. As one test of consistency, we find good agreement between multiple excited-state energies for P6 obtained by DAPS and those obtained by pulsed-gate spectroscopy [11] as shown in Fig. 4(a). In contrast to DAPS,

the latter measurement requires direct loading from an electron reservoir and hence cannot be done on inner dots (like P5) without substantial retuning. The P6 valley splitting inferred from DAPS measurements (162 μeV) and pulsed-gate-spectroscopy measurements (173 μeV) is also close to the largest singlet-triplet splitting of 142 μeV measured by two-electron spin-blockade spectroscopy [17], as
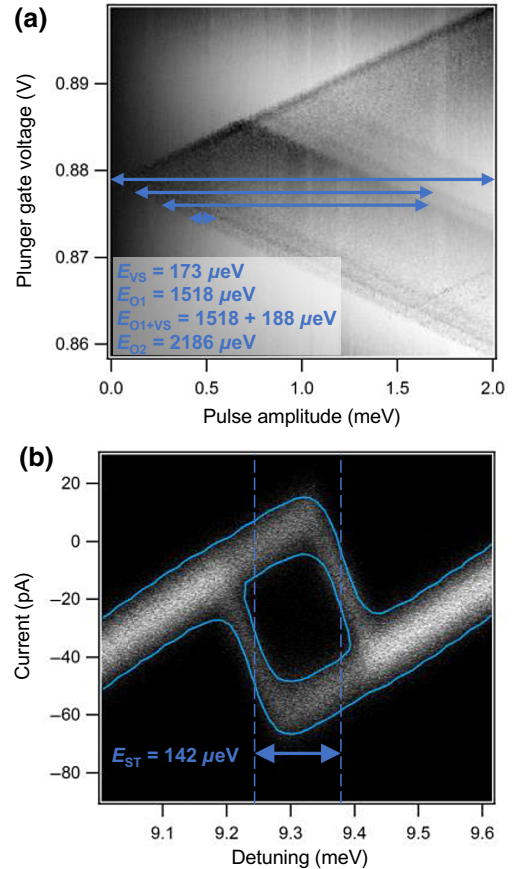

FIG. 4. (a) Pulsed-gate spectroscopy of P6 in a voltage configuration similar to that in Fig. 3(b). The resulting energies [e.g., E_{O1} (E_{O2}) denotes the first (second) orbital excitation] compare favorably to those in Table I, supporting our assignments. (b) Single-shot measurements of the (1,1)-(0,2) transition for P6, showing two-electron singlet-triplet splitting (E_{ST}) from spin-blockade spectroscopy.

shown in Fig. 4(b); this suggests the latter is valley limited in this bias tune-up.

The DAPS method is less susceptible to extraneous resonant tunneling features because electron motion between the dots is not directly coupled to leads. Similar spectroscopic features are consistently seen in many dots (as in Fig. 3), suggesting these are typically true dot features. We try to further suppress coupling with baths by reverse biasing the corresponding barrier gates during DAPS; this does not change the peak features, further confirming they are signs of dot spectroscopy rather than bath loading or unloading. Spurious signals due to fluctuating charges in other (especially accidentally formed) QDs and charge traps are always a possibility, even despite tight control of most of the device surface potential with biased gates, but would be expected to also cause artifacts in charge-stability diagrams and other tuning experiments, which we generally do not observe for the dots measured here.

With this general understanding and confidence in the DAPS technique, we proceed to characterize en masse QDs in several devices fabricated on wafers grown with target QW widths from 3 to 8 nm. The QW widths are confirmed to be close to their targets by x-ray reflectometry. With this larger data set of extracted energies from DAPS, we can examine the reproducibility of measured values across devices from different wafers, dots within each device, excited states within each dot, and variations with heterostructure parameters. Figure 5 compiles the ground-orbital valley splitting from 31 QDs, grouped by wafer. The largest valley splitting here of 286 ± 26 μeV is on par with the highest previously reported in the literature for Si/Si-Ge QDs (which was in a depletion-mode device) [12].

For comparison, we also plot the dependence of valley splitting on well width and interface sharpness as predicted by empirical full-band tight-binding calculations [36]. These calculations assume an unbiased QW, as we expect a small out-of-plane electric field in our devices, and a smooth back interface, as obtained from previous characterization studies [37]. In general, the values fall below the predictions for the atomically sharp interface, suggesting some modest degree of interfacial broadening. While interface sharpness is a convenient modeling parameter, many other factors strongly affect the predicted VS, as discussed in more detail in Appendix D. As a result, the exact sharpness of experimental heterostructures cannot be quantified from the theoretical curves in Fig. 5; the latter are intended only to illustrate the qualitative importance of interface quality for VS. The tendency of measurements from the same wafer to cluster, especially for wider wells, suggests that differences between epitaxial wafers contribute to the observed variation.

Interdot variations in valley splitting are most apparent for the 3-nm-well devices, which is suggestive of increased overlap of the electron wave function in narrower wells
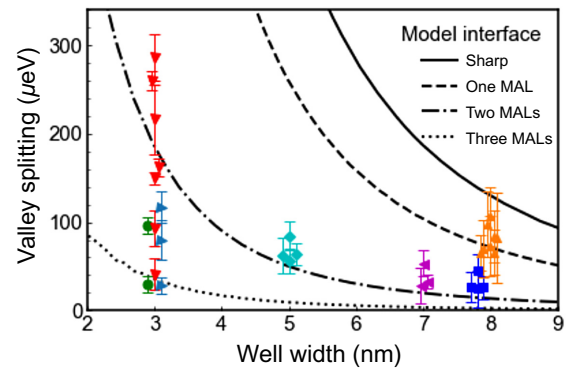

FIG. 5. Ground-orbital valley splittings of 31 QDs from devices across seven wafers differentiated by symbol color and shape. The Si well widths are 3, 5, 7, and 8 nm; QDs with similar VS at the same well width are slightly displaced for clarity. Error bars are extracted from the half width at half maximum of Lorentzian fits of the extracted peaks similar to Figs. 2 and 3. Black curves correspond to tight-binding predictions of valley splitting versus well width as a function of front-interface sharpness in the unit of MALs, as described in the main text and Appendix D.

with a microscopically inhomogeneous interface. This is consistent with the observation in Appendix E that the valley splitting can sometimes vary substantially as the electron is translated along the QW via electrostatic bias [13]. Another consequence of this intradot disorder is that the valley splitting of different orbitals within the same dot also tends to vary, as suggested by Table I and further supported by measurements on multiple dots.
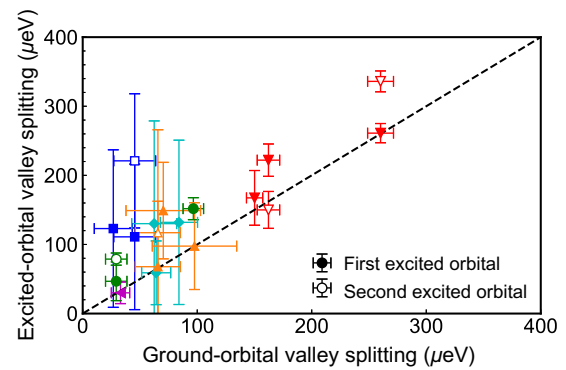

FIG. 6. Measurements of valley splitting in the ground-orbital, first excited-orbital, and second excited-orbital states from six devices from five different wafers where each symbol color and shape corresponds to the same devices as in Fig. 5(a). Error bars are from Lorentzian fits of peak widths. Valley splittings of both the ground state and the first excited-orbital state (filled circles) are measured on 15 dots, while valley splittings of the second exited-orbital state are measured on five dots (empty circles). The diagonal line is included for visual reference to indicate variations in valley splitting between different orbitals.

In Fig. 6, we observe a correlation of valley splitting between ground and excited orbitals, which is notably higher than that between different dots in the same device (Fig. 5). This observation is highly suggestive of greater interface homogeneity on length scales akin to the spatial extent of single electrons (approximately 30 nm from modeling) compared with that of the distance between dots (approximately 150 nm). Curiously, in most cases the excited-orbital valley-splitting values are larger, particularly when the ground-orbital valley splitting is small. We attribute this to systematic bias in resolving high-energy peaks. As noted in Fig. 2(c), excited orbitals generally relax quickly and hence have faster interdot transition rates, broadening the associated DAPS peaks and making it difficult to identify small splittings in the vicinity of multiple orbital excitations.

V. CONCLUSIONS

Using the DAPS technique, we can straightforwardly extract multiple excited-state energies in single-electron quantum dots. From our measurements, we infer distinct ranges of valley splittings (tens of microeleceronvolts to 300 μeV) and orbital splittings (1–2 meV) that are well separated in energy and generally consistent with expectations based on theory, simulations, and prior experimental observations. Auxiliary information, such as the variation of charge decay rates for different transitions, further corroborates our valley-orbit assignments for these states. Definitive interpretation for higher excited states is difficult in some cases where multiple valley and orbital states are similar in energy, as we have taken care to clearly illustrate.

The relative simplicity of the DAPS method allows the probing of valley-splitting disorder within and between QDs as well as different wafers, which will be critical for identifying and improving optimal epitaxial conditions for Si/Si-Ge qubits. The largest splittings we observed were in 3-nm-well devices, and further work is needed to fully understand all other sources of variation. The well widths explored here are narrower than those typically used for Si/Si-Ge qubits in other studies (where they frequently span 8–18 nm) but this does not prevent the formation or hinder the performance of spin qubits [30,38,39]. We also explored the dependence of magnetic dephasing on quantum-well width in separate work [40].

Although we present single-electron measurements in this work, the DAPS technique can be extended to study multielectron state spectra since it relies on the general effects of charge dephasing and relaxation, such as the two-electron spectra extraction discussed in Appendix F. Our approach may also be applicable for studying the rich interplay of the orbital, valley, and spin degrees of freedom in quantum-dot states in other systems besides Si/Si-Ge, such as Si MOS [41], III-V semiconductors [42], or two-dimensional materials [43].

APPENDIX A: DAPS WITH RF TRANSITIONS

Converting applied detuning voltages into energy scales is commonly done by synthesizing separate measurements of gate lever arms and cross-capacitances [17]. This approach, although expedient, is prone to systematic errors. We address this concern by operating the DAPS sequences exactly as described in the main text while also applying a continuous-wave microwave tone to drive photon-assisted-tunneling (PAT) transitions. These experiments reveal PAT transitions in the DAPS spectra [Fig. 7(b)]. By sweeping the frequency of the applied tone
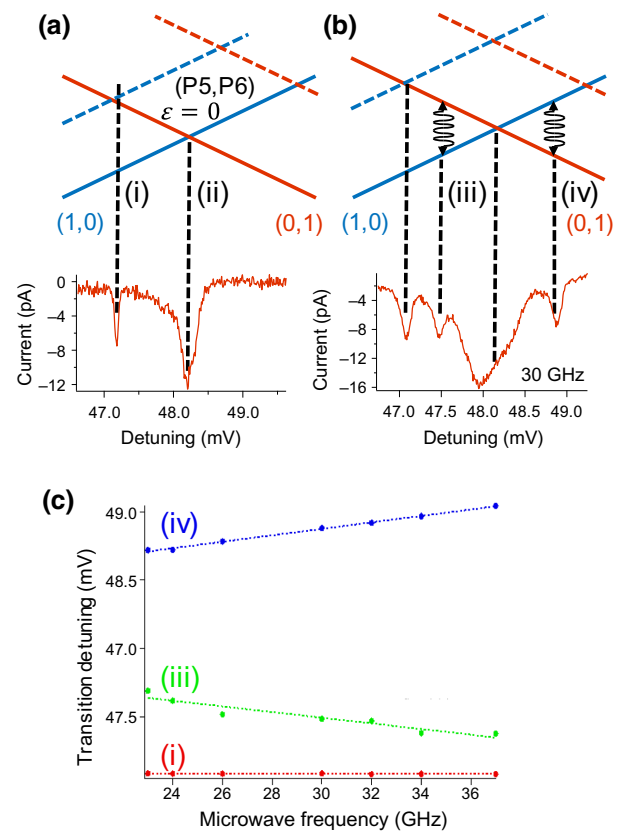

FIG. 7. (a) DAPS spectrum of a QD at a hold time of 5 μs without application of a continuous microwave drive. Transition (i) is the ground-to-excited transition, while (ii) is the ground-to-ground transition. (b) Same experimental pulse sequence at a hold time of 10 μs, with a 30-GHz continuous microwave drive applied through a neighboring gate. Two new transitions, labeled as (iii) and (iv), appear due to photon-assisted tunneling. (c) Tracking transitions (i), (iii), and (iv) versus microwave frequency. The average of the slopes (blue and green) results in a detuning scale factor of 0.186 eV/V.
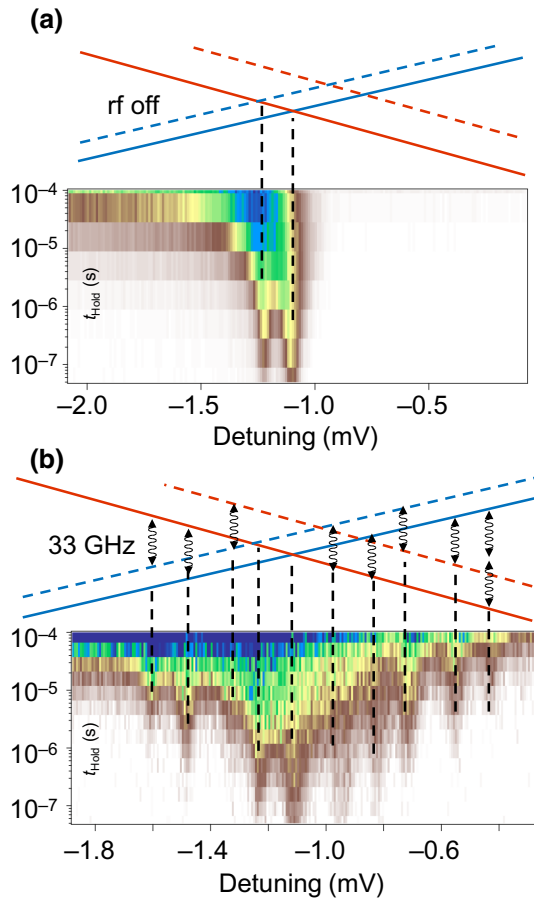
FIG. 8. (a) DAPS measurement at small detunings for a QD without an rf drive. This experimental procedure is identical to the procedures described in the main text. (b) DAPS measurement for thr same QD but with a 33-GHz rf tone applied to a nearby gate. Some two-photon transitions are also visible, whose positions correspond well with the dc and rf resonances expected from the energy-level diagram depicted. The faint transition on the far right potentially corresponds to a two-photon resonance.

[Fig. 7(c)] and fitting a linear slope to the two frequency-dependent transitions, we are able to more accurately convert detuning voltages into an energy scale by using the slope as the so-called detuning scale factor, which has the unit of electronvolts per volt. Our sweeping both the detuning and the hold time with an applied continuous-wave tone reveals even more PAT transitions, whose spacings are consistent with our original interpretation of the transitions as excited states in the dots, as seen in Fig. 8. The visibility of these measurements varies significantly in practice depending on the sensitivity of the QD to applied microwave tones.

APPENDIX B: MODEL OF DAPS DYNAMICS

The main dynamic features of our experiments are captured by a standard Lindblad-master-equation analysis. When a DQD is detuned in the immediate vicinity of an interdot transition, the relevant parameters are the detuning from the anticrossing (ε), the interdot tunnel coupling (t_c), the charge dephasing rate (κ), and inelastic decay (Γ; which is detuning dependent), so the dynamics of the two levels of the anticrossing can be described by the evolution of the density matrix:

$$\dot{\rho}(t) = -i[\varepsilon\sigma_z + t_c\sigma_x, \rho] - \frac{\kappa}{2}(\sigma_z\rho\sigma_z - \rho) + \mathcal{L}_{\Gamma(\varepsilon)}(\rho). \tag{B1}$$

It is straightforward to show that when $\kappa > t_c$ and Γ is ignored, the system decays to a 50:50 mixed charge state at a relaxation rate approximately given by $\kappa t_c^2/(\kappa^2 + \varepsilon^2)$, providing motivation for the use of a Lorentzian fit of the decay rate around each transition for determining the peak position. This yields a peak in the decay rate at the anticrossing, which is the central feature we seek; however, away from the anticrossing, inelastic decay is necessary to thermalize the final state population to equilibrium. We describe the latter with the decay superoperator in Eq. (B1), where the inelastic decay rate Γ can arise from couplings to a variety of environmental degrees of freedom, including evanescent-wave Johnson noise from metal gates and neighboring two-dimensional-electron-gas reservoirs [44] and acoustic phonons in Si [45]. While the precise magnitudes of the lifetimes depend sensitively on device features, we expect that at small detuning, Johnson-noise-induced relaxation will scale as $\Gamma_{JN} \propto t_c^2/\varepsilon$ while phonon-induced relaxation will scale as $\Gamma_{ph} \propto t_c^2\varepsilon^3$. Importantly, this suggests that at small and moderate DQD detuning, the inelastic decay rate may be slower than the dephasing-induced charge decay near excited-state anticrossings, allowing the latter to be resolved. At larger detuning, phonon-induced decay dominates, and its magnitude must include the competing influence of phonon-bottleneck effects, increased phonon density of states, and enhancement of the transition-matrix elements due to the spatially extended wave functions of excited states. Numerical calculations show strong enhancement of inelastic decay in this regime, which can make transitions at excited anticrossings harder to pick out.

To show how these dynamics are relevant to resolving excited-state energies, we extend this model to a three-level calculation of dynamics as a function of detuning and hold time as shown in Fig. 9(a), modeling the DAPS decay of the charge state of one dot into the ground and valley excited states of another dot. The calculations qualitatively reproduce the experimental decay dynamics seen at low detuning in Fig. 9(b) as well as Figs. 3(a) and 3(b). One important feature of both the model and the experimental results, as discussed in Appendix C, is that the locations corresponding to interdot peaks tend to shift toward positive detuning as the hold time increases; this occurs because charge relaxation Γ tends to asymmetrize
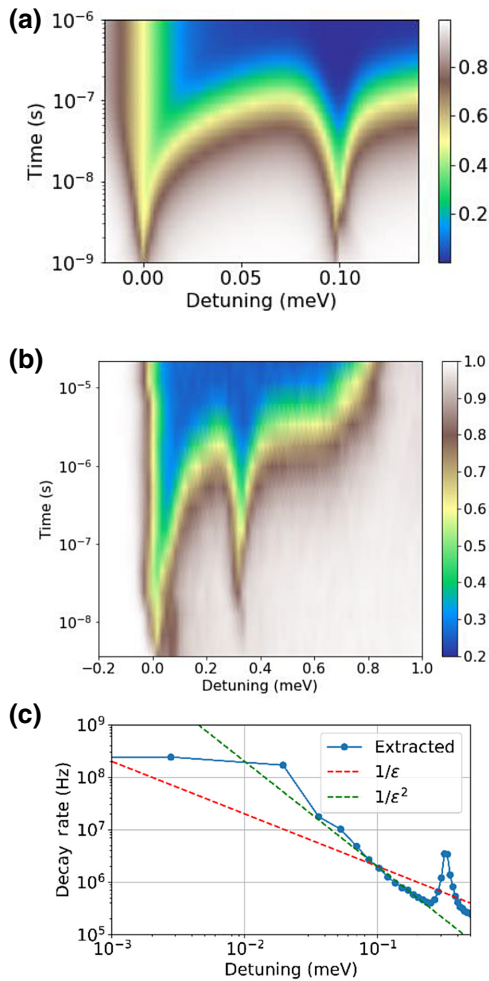
FIG. 9. (a) Theoretically calculated decay of the initial (1,0) charge state as a function of detuning and hold time in a three-level model including ground and valley (0,1) states. (b) DAPS decay measurement for one QD as function of detuning and hold time in the vicinity of the ground orbital and valley transitions. (c) Extracted charge decay rate from data in (b) as a function of detuning; dashed lines are fits to $1/\varepsilon$ and $1/\varepsilon^2$ dependences, showing the latter better matches the experimental dependence at low energies.

the charge-state population by pushing it toward thermalization. As the hold time increases, the detuning location of each peak will therefore be offset from the true anticrossing position, which will usually be located on the rising shoulder of the peak. Therefore, peak positions should ideally be extracted at short hold times for the most-accurate extraction of excited-state energies.

The extracted inelastic decay rates shown in Fig. 9(c) scale as ε^{-2} at small detuning. One possible reason for this discrepancy between the model and the experiment is that some other decay mechanism besides phonons or thermal Johnson noise dominates at very low energies, as other experiments in Si/Si-Ge QDs have also suggested [9,13]. While this model captures the essential features of

the DAPS technique, it ignores important details such as the presence of $1/f$ charge noise, whose effects are not simply parameterized by a Markovian dephasing rate κ and may contribute to nonexponential decay and the broadening of transition peaks in experiments. Recently, a similar model was applied to describe the dynamics during readout in singlet-triplet qubits [46].

APPENDIX C: PEAK ALIGNMENTS FOR A DQD PAIR

The DAPS technique works on a pair of adjacent dots, and irrespective of which dot the reference measurement is performed on, there is only one ground-ground anticrossing for the dot pair. Therefore, when DAPS measurements for both dots are directly compared, the expectation is the ground-ground peak locations in detuning voltage should exactly align. In practice, however, we find that the maxima of the peaks may not be quite aligned with each other, as shown in Fig. 10(a). This detuning offset between the peaks persists even when the measurement is taken in terms of the relative populations between the two charge states [Fig. 10(b)], and suggests the location of
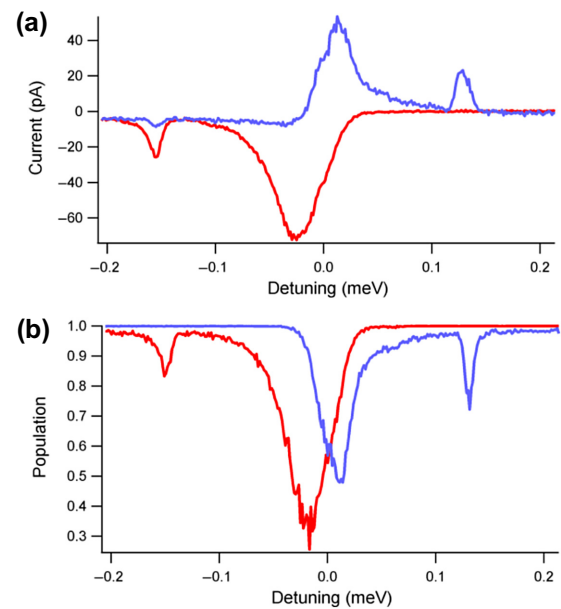

FIG. 10. (a) The P5 (red) and P6 (blue) DAPS sequences at two different hold times (6 and 0.5 μs) have opposite charge signals due to their opposite charge-state references. Comparison of the two reveals a detuning offset between the maxima of the ground-ground transition peaks. (b) P6 and P5 DAPS measurement sequence as in (a) except the lock-in signal is measured in terms of the relative population between the reference charge state and the charge state after dephasing. A value of 1.0 represents 100% of the population remaining in the initial charge state after dephasing at the detuning point (x axis), while 0.0 represents 0% of the initial population remaining in the initial charge state.

the anticrossing is between the onset of the peak and the maximum of the peak. This observation can be explained by asymmetry versus detuning of inelastic charge thermalization Γ and is reproduced by modeling, as discussed in Appendix B, and can also be influenced by nonideal pulses. This provides motivation for our decision to label the uncertainty for each DAPS peak as approximately the half width at half maximum obtained from Lorentzian fits. This error can be reduced by operation at shorter hold times to suppress inelastic decay, at the cost of reduced signal.

APPENDIX D: VALLEY-SPLITTING MODELING

We perform empirical *spds** tight-binding calculations of valley splitting to understand the theoretically expected dependence on well width. Valley-splitting models for Si/Si-Ge QWs frequently assume perfectly abrupt interfaces, which may be interrupted by steps or tilts, as reviewed, for example, in Ref. [3]. In the case of an electron confined by two perfectly abrupt interfaces, the valley splitting oscillates as the QW width changes at the monoatomic-layer (MAL) scale due to intervalley phase interference [22,23,47]. In general, however, growth kinetics and atomic diffusion during epitaxy and device fabrication will broaden the interfaces, as confirmed by microscopy and atom-probe tomography [37]. These measurements suggest that the back interface is typically broader than the front interface, which would suppress valley interferometric effects as a function of the well width. Additional asymmetries, such as the presence of a strong electric field, would similarly depress valley oscillations.

Our tight-binding calculations use the parameters for bulk Si and Ge in Ref. [36], with the $Si_{0.7}Ge_{0.3}$ layers described within the virtual-crystal approximation. We model each QW interface using a sigmoidal function for the Ge concentration:

$$\chi_{\pm}(x) = \frac{\chi_{\text{Si-Ge}}}{1 + e^{(x_{0,\pm} \pm x)/\tau_{\pm}}}, \qquad \text{(D1)}$$

where $x_{0,\pm}$ denotes the interface position and $\tau_{\pm}$ is the interface width parameter for the front and back interfaces, respectively; 4τ is the distance over which the Ge percentage varies from 12% to 88% of its value in the barrier region $\chi_{\text{Si-Ge}}$. We fix $4\tau_{-}$ for the back interface at eight MALs, following the extracted values in Ref. [37], and vary the sharpness of the front interface $4\tau_{+}$ between zero and three MALs to obtain the results shown in Fig. 5. Zero applied vertical electric field is assumed, since electrostatic simulations of our devices indicate a negligible field under typical operating conditions. In general, a finite positive electric field will tend to increase the valley splitting as the electron overlaps more strongly with the sharp front interface; this effect is more prominent for wider wells.

While τ_{+} of the front interface is the only free parameter in our calculations, in practice a large number of additional factors will affect the predicted VS values. Our calculations are for one-dimensional QW structures and thus do not include disorder effects beyond the homogeneous smoothing of the interfaces; such disorder would further broaden the expected VS distribution [26]. Additionally, while the empirical tight-binding parameters for Si and Ge are obtained by fitting to bulk band-structure features, multiple parametrizations are possible, and the relevant intervalley coupling is not uniquely constrained at present. In our experience, commonly used Si and Ge *spds** tight-binding-parameter sets in the literature [20,48,49] can lead to variations of up to 2 times in predicted VS. Furthermore, any true heterostructure is ultimately composed of substitutional Ge atoms in the barrier regions and therefore also includes local strain. Three-dimensional atomistic calculations including these effects can lead to differences from one-dimensional virtual-crystal-approximation models (as discussed in the supplemental section of Ref. [3], for example). Because of the quantitative importance of and uncertainty in these and other factors, these calculations are intended to serve only as a qualitative indicator of the sensitivity of VS to interface effects and not as an attempt to quantify interface sharpness τ using measured VS values.

APPENDIX E: VALLEY-SPLITTING DEPENDENCE ON ELECTROSTATIC BIAS

To observe the sensitivity of energy splittings on the electrostatic confinement, we can evaluate how much DAPS transitions are affected by changing the bias of a nearby gate (typically a neighboring tunneling barrier), which alters the convexity of the potential confinement along one of the two spatial directions and causes lateral displacement of the quantum dot along that same direction. In the ideal scenario, we expect orbital-like transitions to be more sensitive to these changes than valley-like transitions. However, the valley mixing can also experience substantial changes as the electron is translated along a microscopically varying heterointerface, due to some combination of disorder effects such as interfacial steps and/or intrinsic atomistic random alloy fluctuations. In Fig. 11 we observe that two neighboring dots (P5 and P6 in a device) exhibit very different behavior in the measured VS as a function of bias on different adjacent gates; P5 shows a significant change (by about a factor of 3 within the probed bias range), while its neighboring dot retains a roughly constant VS. This illustrates both the importance of local microscopic disorder on the VS and the possibility that such disorder can be uncorrelated between different dots. The trends we detect in bias tunability of VS are consistent with previous observations in the literature [13,50].
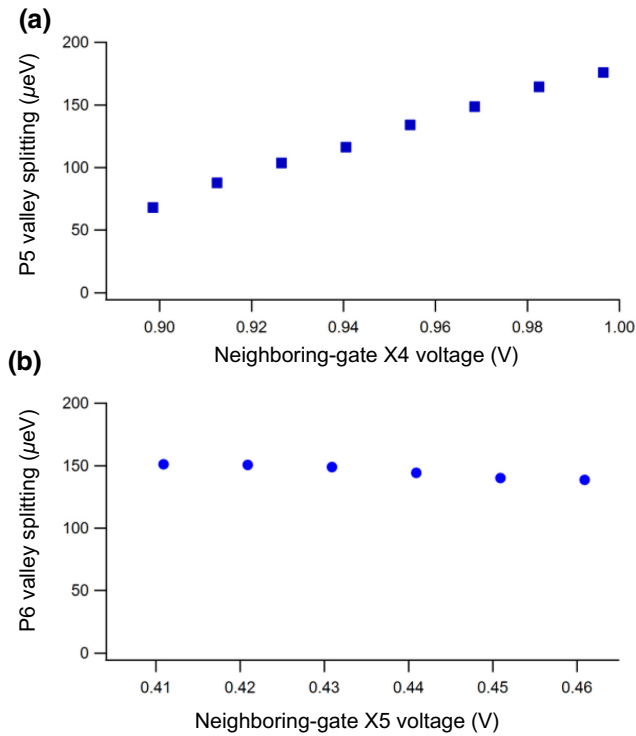
FIG. 11. Variation of valley splitting on either side of a P5-P6 DQD for (a) a P5 electron as function of bias on an X4 gate and (b) a P6 electron as a function of bias on an X5 gate.
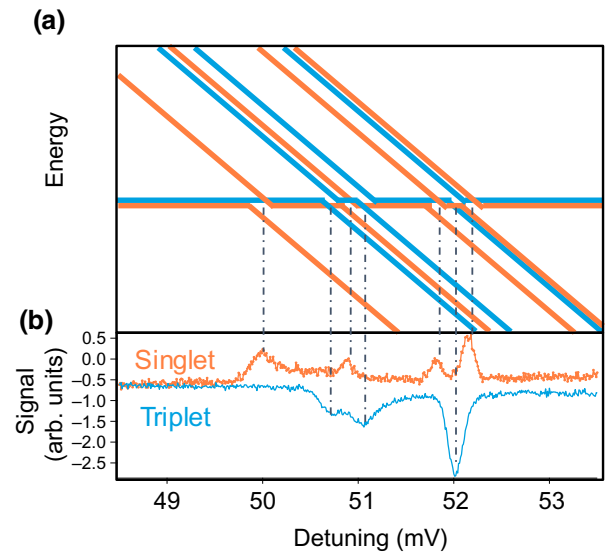

FIG. 12. (a) Two-electron eigenenergies near the (1,1)-(2,0) charge transition, allowing for valleys and excited orbitals. (b) Measured spin-dependent spectra of two-electron states. Singlets in orange, triplets in blue.

APPENDIX F: TWO-ELECTRON DAPS

While one-electron spectra are most transparent for understanding dot confinement, valley splitting, and decoherence pathways of single spins in dots, it is the energies of two-electron eigenstates that affect the fidelities of the spin initialization and readout in spin-qubit proposals. The DAPS technique can be readily applied to this case, and many useful variants can be envisioned. In particular, the singlet and triplet spectra of a two-electron QD can be selectively probed in different ways with use of either a DQD device or a triple-QD device.

A simple DQD experiment could initialize a (2,0) ground singlet, adiabatically separate it to the (1,1) state, and then diabatically pulse along the detuning axis, scanning for resonances with two-electron states of either one dot—when going toward (2,0)—or the other dot [toward (0,2)]. Because of spin conservation, this would predominantly probe singlets. This pulse sequence could be modified by adding a wait time $t_{\mathrm{dephasing}}$ after adiabatic separation of the singlet. When $t_{\mathrm{dephasing}}$ is comparable to the singlet-triplet dephasing lifetime T_2^*, both singlets and triplets should become accessible during the scan along the detuning axis. However, crowding of states and conflicting optimal t_{hold} values for different states can complicate extraction of the energy levels.

Alternatively, with a third dot we can form an exchange-only qubit [28,30] that we can electrically manipulate to separately map out the two-electron singlet and triplet eigenstates of a singlet dot, as shown in Fig. 12. The sequence of steps for these experiments is very similar to that outlined above. As an example, the dots underneath plungers (P6, P5, P4) are operated around the (2,0,1)-(1,1,1) charge transition. A spin singlet is first initialized in the P6 dot and then adiabatically ramped into the (1,1,1) charge cell. From this point, diabatic detuning pulses toward P6 result in two-electron eigenstates of the P6 dot (or P5 if we are going in the opposite direction along the detuning axis) coming into and out of resonance with the P6 or P5 (1,1) singlet state. Dephasing at the anticrossing points followed by a diabatic pulse back into the (1,1,1) charge configuration results in a charge-state-dependent outcome. The charge-state measurement is subtracted from the result in a second round of reinitialization followed by a charge-state measurement. The resulting lock-in measurement for increasingly larger detuning pulses toward the P6 dot results in a series of peaks where the (1,1) singlet level crosses the two-electron spin-singlet eigenstates in P6. This measurement would be the same as in a DQD experiment, resulting in the orange line in Fig. 12(b) with pronounced singlet peaks. Additionally, in a triple-QD qubit, a composite X_π Clifford gate using exchange pulses can be inserted after initialization to prepare an entangled three-spin state that is projected only onto P6 or P5 (1,1) triplet states. Subsequent diabatic detuning pulses into P6 then reveal only the resonances between the (1,1) triplets with two-electron spin-triplet eigenstates in P6 [Fig. 12(b),

blue line]. The spin-singlet and spin-triplet spectra of the P6 dot can be compared to determine whether valley or orbital states are limiting the lowest singlet-triplet energy splitting [35], and to assess the degree of valley-orbit coupling present in the dot.

———

[1] L. M. K. Vandersypen and M. A. Eriksson, Quantum computing with semiconductor spins, Phys. Today **72**, 38 (2019).

[2] T. D. Ladd and M. S. Carroll, in *Encyclopedia of Modern Optics* (Elsevier, Oxford, 2018) 2nd ed., p. 467.

[3] F. A. Zwanenburg, A. S. Dzurak, A. Morello, M. Y. Simmons, L. C. L. Hollenberg, G. Klimeck, S. Rogge, S. N. Coppersmith, and M. A. Eriksson, Silicon quantum electronics, Rev. Mod. Phys. **85**, 961 (2013).

[4] S. Goswami, K. A. Slinker, M. Friesen, L. M. McGuire, J. L. Truitt, C. Tahan, L. J. Klein, J. O. Chu, P. M. Mooney, D. W. Van Der Weide, R. Joynt, S. N. Coppersmith, and M. A. Eriksson, Controllable valley splitting in silicon quantum devices, Nat. Phys. **3**, 41 (2007).

[5] K. Sasaki, R. Masutomi, K. Toyama, K. Sawano, Y. Shiraki, and T. Okamoto, Well-width dependence of valley splitting in Si/SiGe quantum wells, Appl. Phys. Lett. **95**, 222109 (2009).

[6] S. F. Neyens, R. H. Foote, B. Thorgrimsson, T. J. Knapp, T. McJunkin, L. M. K. Vandersypen, P. Amin, N. K. Thomas, J. S. Clarke, D. E. Savage, M. G. Lagally, M. Friesen, S. N. Coppersmith, and M. A. Eriksson, The critical role of substrate disorder in valley splitting in Si quantum wells, Appl. Phys. Lett. **112**, 243107 (2018).

[7] B. P. Wuetz, M. P. Losert, A. Tosato, M. Lodari, P. L. Bavdaz, L. Stehouwer, P. Amin, J. S. Clarke, S. N. Coppersmith, A. Sammak, M. Veldhorst, M. Friesen, and G. Scappucci, arXiv:2006.02305 (2020).

[8] M. Fuechsle, S. Mahapatra, F. A. Zwanenburg, M. Friesen, M. A. Eriksson, and M. Y. Simmons, Spectroscopy of few-electron single-crystal silicon quantum dots, Nat. Nanotechnol. **5**, 502 (2010).

[9] K. Wang, C. Payette, Y. Dovzhenko, P. W. Deelman, and J. R. Petta, Charge Relaxation in a Single-Electron Si/SiGe Double Quantum Dot, Phys. Rev. Lett. **111**, 046801 (2013).

[10] X. Mi, C. G. Péterfalvi, G. Burkard, and J. R. Petta, High-Resolution Valley Spectroscopy of Si Quantum Dots, Phys. Rev. Lett. **119**, 176803 (2017).

[11] J. M. Elzerman, R. Hanson, L. H. Willems van Beveren, L. M. K. Vandersypen, and L. P. Kouwenhoven, Excited-state spectroscopy on a nearly closed quantum dot via charge detection, Appl. Phys. Lett. **84**, 4617 (2004).

[12] M. G. Borselli, R. S. Ross, A. A. Kiselev, E. T. Croke, K. S. Holabird, P. W. Deelman, L. D. Warren, I. Alvarado-Rodriguez, I. Milosavljevic, F. C. Ku, W. S. Wong, A. E. Schmitz, M. Sokolich, M. F. Gyure, and A. T. Hunter, Measurement of valley splitting in high-symmetry Si/SiGe quantum dots, Appl. Phys. Lett. **98**, 123118 (2011).

[13] A. Hollmann, T. Struck, V. Langrock, A. Schmidbauer, F. Schauer, K. Sawano, H. Riemann, N. V. Abrosimov, D. Bougeard, and L. R. Schreiber, Large and Tunable Valley Splitting in Si/SiGe Quantum Dots, Phys. Rev. Appl. **13**, 034068 (2020).

[14] D. Harbusch, S. Manus, H. P. Tranitz, W. Wegscheider, and S. Ludwig, Radio frequency pulsed-gate charge spectroscopy on coupled quantum dots, Phys. Rev. B **82**, 195310 (2010).

[15] H. Hubel, C. D. Nugroho, A. Morello, C. C. Escott, M. A. Eriksson, C. Yang, D. N. Jamieson, R. G. Clark, and A. S. Dzurak, Electron tunnel rates in a donor-silicon single electron transistor hybrid, Phys. Rev. B **81**, 235318 (2010).

[16] C. B. Simmons, J. R. Prance, B. J. Van Bael, T. S. Koh, Z. Shi, D. E. Savage, M. G. Lagally, R. Joynt, M. Friesen, S. N. Coppersmith, and M. A. Eriksson, Tunable Spin Loading and T_1 of a Silicon Spin Qubit Measured by Single-Shot Readout, Phys. Rev. Lett. **106**, 156804 (2011).

[17] A. M. Jones, E. J. Pritchett, E. H. Chen, T. E. Keating, R. W. Andrews, J. Z. Blumoff, L. A. De Lorenzo, K. Eng, S. D. Ha, A. A. Kiselev, S. M. Meenehan, S. T. Merkel, J. A. Wright, L. F. Edge, R. S. Ross, M. T. Rakher, M. G. Borselli, and A. Hunter, Spin-Blockade Spectroscopy of Si/Si-Ge Quantum Dots, Phys. Rev. Appl. **12**, 014026 (2019).

[18] J. S. Schoenfield, B. M. Freeman, and H. W. Jiang, Coherent manipulation of valley states at multiple charge configurations of a silicon quantum dot device, Nat. Commun. **8**, 1 (2017).

[19] N. E. Penthorn, J. S. Schoenfield, J. D. Rooney, L. F. Edge, and H. W. Jiang, Two-axis quantum control of a fast valley qubit in silicon, npj Quantum Inf. **5**, 1 (2019).

[20] T. B. Boykin, G. Klimeck, M. A. Eriksson, M. Friesen, S. N. Coppersmith, P. Von Allmen, F. Oyafuso, and S. Lee, Valley splitting in strained silicon quantum wells, Appl. Phys. Lett. **84**, 115 (2004).

[21] T. B. Boykin, G. Klimeck, M. Friesen, S. N. Coppersmith, P. von Allmen, F. Oyafuso, and S. Lee, Valley splitting in low-density quantum-confined heterostructures studied using tight-binding models, Phys. Rev. B **70**, 165325 (2004).

[22] M. Friesen, S. Chutia, C. Tahan, and S. N. Coppersmith, Valley splitting theory of SiGe/Si/SiGe quantum wells, Phys. Rev. B **75**, 115318 (2007).

[23] L. Zhang, J.-W. Luo, A. Saraiva, B. Koiller, and A. Zunger, Genetic design of enhanced valley splitting towards a spin qubit in silicon, Nat. Commun. **4**, 1 (2013).

[24] N. M. Zimmerman, P. Huang, and D. Culcer, Valley phase and voltage control of coherent manipulation in Si quantum dots, Nano Lett. **17**, 4461 (2017).

[25] N. Kharche, M. Prada, T. B. Boykin, and G. Klimeck, Valley splitting in strained silicon quantum wells modeled with 2 miscuts, step disorder, and alloy disorder, Appl. Phys. Lett. **90**, 092109 (2007).

[26] Z. Jiang, N. Kharche, T. Boykin, and G. Klimeck, Effects of interface disorder on valley splitting in SiGe/Si/SiGe quantum wells, Appl. Phys. Lett. **100**, 103502 (2012).

[27] J. K. Gamble, M. A. Eriksson, S. N. Coppersmith, and M. Friesen, Disorder-induced valley-orbit hybrid states in Si quantum dots, Phys. Rev. B **88**, 035310 (2013).

[28] D. P. DiVincenzo, D. Bacon, J. Kempe, G. Burkard, and K. B. Whaley, Universal quantum computation with the exchange interaction, Nature **408**, 339 (2000).

[29] M. D. Reed, B. M. Maune, R. W. Andrews, M. G. Borselli, K. Eng, M. P. Jura, A. A. Kiselev, T. D. Ladd, S. T. Merkel, I. Milosavljevic, E. J. Pritchett, M. T. Rakher, R. S. Ross, A. E. Schmitz, A. Smith, J. A. Wright, M. F. Gyure, and A. T. Hunter, Reduced Sensitivity to Charge Noise in Semiconductor Spin Qubits via Symmetric Operation, Phys. Rev. Lett. **116,** 110402 (2016).

[30] R. W. Andrews, C. Jones, M. D. Reed, A. M. Jones, S. D. Ha, M. P. Jura, J. Kerckhoff, M. Levendorf, S. Meenehan, S. T. Merkel, A. Smith, B. Sun, A. J. Weinstein, M. T. Rakher, T. D. Ladd, and M. G. Borselli, Quantifying error and leakage in an encoded Si/SiGe triple-dot qubit, Nat. Nanotechnol. **14,** 747 (2019).

[31] M. G. Borselli, K. Eng, R. S. Ross, T. M. Hazard, K. S. Holabird, B. Huang, A. A. Kiselev, P. W. Deelman, L. D. Warren, I. Milosavljevic, A. E. Schmitz, M. Sokolich, M. F. Gyure, and A. T. Hunter, Undoped accumulation-mode Si/SiGe quantum dots, Nanotechnology **26,** 375202 (2015).

[32] B. M. Maune, M. G. Borselli, B. Huang, T. D. Ladd, P. W. Deelman, K. S. Holabird, A. A. Kiselev, I. Alvarado-Rodriguez, R. S. Ross, A. E. Schmitz, M. Sokolich, C. A. Watson, M. F. Gyure, and A. T. Hunter, Coherent singlet-triplet oscillations in a silicon-based double quantum dot, Nature **481,** 344 (2012).

[33] Adiabatic and diabatic pulses refer to the two extreme conditions of Landau-Zener transitions [18,34].

[34] X. Mi, S. Kohler, and J. R. Petta, Landau-zener interferometry of valley-orbit states in Si/SiGe double quantum dots, Phys. Rev. B **98,** 161404 (2018).

[35] D. Culcer, L. Cywiński, Q. Li, X. Hu, and S. Das Sarma, Quantum dot spin qubits in silicon: Multivalley physics, Phys. Rev. B **82,** 155312 (2010).

[36] Y.-M. Niquet, D. Rideau, C. Tavernier, H. Jaouen, and X. Blase, Onsite matrix elements of the tight-binding hamiltonian of a strained crystal: Application to silicon, germanium, and their alloys, Phys. Rev. B **79,** 245201 (2009).

[37] O. Dyck, D. N. Leonard, L. F. Edge, C. A. Jackson, E. J. Pritchett, P. W. Deelman, and J. D. Poplawsky, Accurate quantification of Si/SiGe interface profiles via atom probe tomography, Adv. Mater. Int. **4,** 1700622 (2017).

[38] B. Sun, Full permutation dynamical decoupling in an encoded triple-dot qubit, Bull. Am. Phys. Soc. **65** (2020).

[39] J. Blumoff, Quantifying high-fidelity state preparation and measurement in triple-quantum-dot qubits, Bull. Am. Phys. Soc. **65** (2020).

[40] J. Kerckhoff, B. Sun, B. H. Fong, C. Jones, A. A. Kiselev, D. W. Barnes, R. S. Noah, E. Acuna, M. Akmal, S. D. Ha, J. A. Wright, B. J. Thomas, C. A. C. Jackson, L. F. Edge, K. Eng, R. S. Ross, and T. D. Ladd, arXiv:2009:08079 (2020).

[41] J. K. Gamble, P. Harvey-Collard, N. T. Jacobson, A. D. Baczewski, E. Nielsen, L. Maurer, I. Montaño, M. Rudolph, M. S. Carroll, C. H. Yang, A. Rossi, A. Dzurak, and R. P. Muller, Valley splitting of single-electron SiMOS quantum dots, Appl. Phys. Lett. **109,** 253101 (2016).

[42] J. R. Petta, A. C. Johnson, C. M. Marcus, M. P. Hanson, and A. C. Gossard, Manipulation of a Single Charge in a Double Quantum Dot, Phys. Rev. Lett. **93,** 186802 (2004).

[43] K. Wang, K. De Greve, L. A. Jauregui, A. Sushko, A. High, Y. Zhou, G. Scuri, T. Taniguchi, K. Watanabe, M. D. Lukin, H. Park, and P. Kim, Electrical control of charged carriers and excitons in atomically thin materials, Nat. Nanotechnol. **13,** 128 (2018).

[44] L. S. Langsjoen, A. Poudel, M. G. Vavilov, and R. Joynt, Qubit relaxation from evanescent-wave johnson noise, Phys. Rev. A **86,** 010301 (2012).

[45] C. Tahan and R. Joynt, Relaxation of excited spin, orbital, and valley qubit states in ideal silicon quantum dots, Phys. Rev. B **89,** 075302 (2014).

[46] A. E. Seedhouse, T. Tanttu, R. C. C. Leon, R. Zhao, K. Y. Tan, B. Hensen, F. E. Hudson, K. M. Itoh, J. Yoneda, C. H. Yang, A. Morello, A. Laucht, S. N. Coppersmith, A. Saraiva, and A. S. Dzurak, Pauli blockade in silicon quantum dots with spin-orbit control, PRX Quantum **2,** 10303 (2021).

[47] M. O. Nestoklon, E. L. Ivchenko, J.-M. Jancu, and P. Voisin, Electric field effect on electron spin splitting in SiGe/Si quantum wells, Phys. Rev. B **77,** 155328 (2008).

[48] J.-M. Jancu and P. Voisin, Tetragonal and trigonal deformations in zinc-blende semiconductors: A tight-binding point of view, Phys. Rev. B **76,** 115202 (2007).

[49] F. Sacconi, A. Di Carlo, P. Lugli, M. Stadele, and J.-M. Jancu, Full band approach to tunneling in MOS structures, IEEE Trans. Electron Devices **51,** 741 (2004).

[50] Z. Shi, C. B. Simmons, D. R. Ward, J. R. Prance, R. T. Mohr, T. S. Koh, J. K. Gamble, X. Wu, D. E. Savage, M. G. Lagally, M. Friesen, S. N. Coppersmith, and M. A. Eriksson, Coherent quantum oscillations and echo measurements of a Si charge qubit, Phys. Rev. B **88,** 075416 (2013).